Ceramics International xxx (xxxx) xxx

Contents lists available at ScienceDirect

Ceramics International

journal homepage: www.elsevier.com/locate/ceramint

Thermal, mechanical and optical properties of transparent AlON, MgAlON and $MgAl_2O_4$ ceramics

T.G. Akopdzhanyan [a,c,*], D.I. Abzalov [a], D.A. Agarkov [b,e], E.V. Tsipis [b], D.S. Katrich [b], M.I. Petrzhik [c], K.A. Shcherbakova [c,d], V.V. Grachev [a]

[a] Merzhanov Institute of Structural Macrokinetics and Materials Science RAS, 8 Academician Osipyan str., Chernogolovka, Moscow Region, 142432, Russia
[b] Osipyan Institute of Solid State Physics RAS, 2 Academician Osipyan str., Chernogolovka, Moscow Region, 142432, Russia
[c] National University of Science and Technology MISIS, NUST MISIS, 4 Leninsky prospect, Moscow, 119049, Russia
[d] JSC Federal State Research and Design Institute of Rare Metal Industry (Giredmet), 2 Elektrodnaya st., Moscow, 111524, Russia
[e] Moscow Institute of Physics and Technology, 9 Institutskiy per., Dolgoprudniy, Moscow Region, 1417071, Russia

ARTICLE INFO

Keywords:
Combustion synthesis
Transparent ceramics
Oxynitride
MgAlON
AlON
$MgAl_2O_4$

ABSTRACT

The pressureless sintering behavior of AlON, $MgAl_2O_4$ (MAS), and MgAlON powders produced via self-propagating high-temperature synthesis was investigated at 1830–1930 °C using various sintering aids. As the composition shifted from AlON to MAS, the sintering temperature required for full densification decreased, while the average linear thermal expansion coefficients (TECs) and thermal conductivity increased. Conversely, both hardness and fracture toughness decreased. At 200-1000 °C, the TECs varied in the ranges from (7.5-9.1) × 10^{-6} K^{-1} for AlON to (8.3-9.6) × 10^{-6} K^{-1} for MAS, increasing on heating. The thermal conductivity coefficient reached up to 19 ± 1.5 $Wm^{-1}K^{-1}$ at 25 °C. The light transmittance of the ceramics was up to 57% for AlON, up to 51% for MgAlON, and up to 61% for MAS in the IR spectrum. The influence of different sintering additives on densification and in-line transmittance was also evaluated.

1. Introduction

Transparent ceramics based on the AlN-Al_2O_3-MgO system have attracted considerable attention due to their potential applications in infrared windows and laser ceramics, as well as the automotive and aerospace industries [1–3]. These materials demonstrate a unique combination of high strength, hardness, and optical transparency from the near-UV to the near-IR regions [2,3]. Three materials in this system are particularly prominent: aluminum oxynitride (AlON), magnesium-aluminum oxynitride (MgAlON), and magnesium aluminate spinel ($MgAl_2O_4$, hereafter referred to as MAS). Despite their similarities in crystal structure and application fields, the approaches to powder synthesis and ceramic consolidation differ significantly for each material.

Two main approaches are widely used to obtain AlON powders for further consolidation: carbothermal reduction and nitriding (CRN) [4–6] and solid-state synthesis using Al_2O_3 and AlN precursors [7]. Both approaches require high temperatures (>1700 °C) and prolonged holding times (>2 h) in a nitrogen atmosphere, resulting in substantial energy consumption and particle coarsening. The same approaches are widely used for synthesizing MgAlON powders with different compositions. The main difference lies in the introduction of magnesium oxide into the initial mixtures [8–10]. Magnesium aluminate spinel can be produced using various methods, including solid-state synthesis (>1200 °C, long holding times) [11–14], sol-gel processing (multi-step, labor-intensive) [15–18], and solution combustion synthesis [19–21]. Common drawbacks of all these methods are high energy consumption and long processing times.

In this context, self-propagating high-temperature synthesis (SHS) offers an attractive alternative. Recently, we have developed approaches for producing single-phase AlON [22,23], MgAlON with a controlled composition [24], and MAS powders using SHS with $Mg(ClO_4)_2$ as an internal oxidizer. It was demonstrated that SHS yields fine, weakly agglomerated powders with good sinterability.

Different strategies are employed for consolidation into transparent ceramics, depending on the material. AlON ceramics are most frequently fabricated by pressureless sintering in a nitrogen atmosphere at temperatures of 1800–1950 °C [25,26], using sintering aids such as Y_2O_3

* Corresponding author. Merzhanov Institute of Structural Macrokinetics and Materials Science RAS, 8 Academician Osipyan str., Chernogolovka, Moscow Region, 142432, Russia.
E-mail addresses: tigj@yandex.ru, Tigran@ism.ac.ru (T.G. Akopdzhanyan).

https://doi.org/10.1016/j.ceramint.2026.05.131
Received 22 February 2026; Received in revised form 16 April 2026; Accepted 8 May 2026
Available online 10 May 2026

Table 1
The calculated composition of SHS-derived powders.

Composition	Calculated formulation	AlN, wt. %	Al_2O_3, wt. %	MgO, wt. %
AlON	$Al_{23}O_{27}N_5$	18.24	81.76	0
MgAlON M25	$Mg_{0.28}Al_{2.93}O_{3.9}N_{0.52}$	13.68	79.28	7.04
MgAlON M50	$Mg_{0.53}Al_{2.6}O_{3.93}N_{0.34}$	9.12	76.79	14.09
MgAlON M75	$Mg_{0.77}Al_{2.29}O_{3.97}N_{0.16}$	4.56	74.31	21.13
MAS	$MgAl_2O_4$	0	71.83	28.17

[27], $CaCO_3$ [26], or oxide mixtures [28]. In the case of MgAlON, many studies employ a two-step approach, involving pressureless sintering followed by hot isostatic pressing (HIP) [29,30], although single-step pressureless sintering was also reported [31]. The fabrication of transparent MAS ceramics typically requires pressure-assisted techniques, such as HIP [32], hot pressing [33], or spark plasma sintering (SPS) [34].

Despite the progress in both synthesis and consolidation of these materials, several important gaps remain in the literature. Although each of these materials has been investigated individually, there are no systematic comparative studies of AlON, MgAlON, and MAS ceramics prepared under similar conditions using powders derived from the same synthesis method. Such a comparison is essential for understanding the structure-property relationships across the Al_2O_3-AlN-MgO system and for guiding material selection for specific applications. Furthermore, the potential of SHS-derived powders for producing transparent ceramics remains unexplored. Although SHS has been used to produce powders of these materials, there are no reports on the fabrication of transparent ceramics from SHS-derived AlON, MgAlON, and MAS powders using pressureless sintering. Additionally, the role of sintering aids across different compositions is not well understood. Different additives (Y_2O_3, $CaCO_3$, LiF, and oxide mixtures) have been reported for each material. However, their effectiveness has not been compared under identical processing conditions. It remains unclear whether a universal additive exists that is suitable for all compositions in this system. Finally, the relationship between composition and properties requires a systematic investigation. The effect of composition on the thermal, mechanical, and optical properties of MgAlON solid solutions has not been thoroughly characterized, particularly for materials prepared by pressureless sintering without HIP.

The present study addresses these issues by providing the first systematic comparative investigation of AlON, MgAlON (with three different compositions), and MAS transparent ceramics, all derived from SHS-synthesized powders and consolidated by pressureless sintering under identical conditions. This work has three specific objectives: (1) to characterize the phase composition, morphology, and specific surface area of the SHS-derived powders; (2) to investigate the pressureless sintering behavior of these powders at different temperatures (1830–1930 °C) and with different sintering additives (Y_2O_3, $CaCO_3$, LiF, and a Y_2O_3/La_2O_3/MgO mixture) to establish the optimal consolidation conditions for each composition; (3) to perform a comprehensive characterization of the resulting ceramics, including their optical transmittance, thermal expansion coefficients, thermal conductivity, hardness, Young's modulus, and fracture toughness.

This study provides valuable guidance for the development of transparent ceramics for infrared optical applications and demonstrates the potential of combustion-synthesized powders as precursors for high-performance transparent ceramic materials by systematically comparing these materials prepared from SHS-derived powders under identical conditions.

2. Materials and methods

2.1. Synthesis of powders

Aluminum oxynitride (AlON) was synthesized from aluminum powder (99% purity, an average particle size of 5 μm), aluminum oxide powder (99.999% purity, an average particle size of 1 μm), and magnesium perchlorate (99.99% purity, <40 μm), which served as initial precursors. The component ratios were calculated for the formation of 35.7 mol. % AlN and 64.3 mol. % Al_2O_3. This resulted in an aluminum content below 13 wt % in the Al-Al_2O_3 system for combustion in nitrogen, which is well below the combustion limits. Hence, the synthesis of aluminum oxynitride using the SHS method requires the introduction of an oxidizer into the initial mixture and the replacement of part of Al_2O_3 with Al powder and magnesium perchlorate. Additional heat was released as a result of aluminum oxidation by magnesium perchlorate. Mixtures of Al, Al_2O_3, and $Mg(ClO_4)_2$ were prepared to obtain single-phase AlON via combustion synthesis.

Accordingly, two primary exothermic reactions occurred during synthesis: aluminum nitriding and aluminum oxidation (1):

$$\begin{cases} 16Al + 3Mg(ClO_4)_2 = 8Al_2O_3 + 3MgCl_2 + Q \\ 2Al + N_2 = 2AlN + Q \end{cases} \quad (1)$$

The synthesis was carried out in an SHS reactor at an initial nitrogen pressure of 8 MPa. Details on AlON synthesis in the combustion mode can be found in Refs. [22,35]. The combustion temperature was 1780 °C and the combustion front velocity was 1.2 mm/s.

Mixtures consisting of aluminum powder (99% purity, an average particle size of 5 μm), aluminum oxide powder (99.999% purity, an average particle size of 1 μm), magnesium oxide powder (99.9% purity, a particle size of 1 μm), and magnesium perchlorate (99.99% purity, <40 μm) served as the initial precursors for the synthesis of magnesium-aluminum oxynitride (MgAlON). The compositions of the mixtures were calculated so that aluminum oxynitride (35.7 mol % AlN and 64.3 mol % Al_2O_3) and magnesium aluminate spinel (50 mol % MgO and 50 mol % Al_2O_3) were formed in the combustion front in selected proportions containing 25, 50, or 75 wt % magnesium aluminate spinel (balance AlON) with subsequent formation of MgAlON labeled as M25, M50, and M75, respectively. The nominal compositions of MgAlON are summarized in Table 1. An increase in the calculated amount of MAS in MgAlON led to a decrease in the amount of aluminum involved in the nitriding reaction in the mixture. In our previous work [24], we determined the component ratios necessary to obtain single-phase MgAlON powders. It was also found that a lower combustion temperature was required to obtain compositions with a high magnesium oxide content, which had a positive effect on the specific surface area of the powders.

A mixture consisting of Mg (MPF-4 grade, an average particle size of 60 μm), Al_2O_3 (99.999% purity, an average particle size of 1 μm), MgO (99.9% purity, a particle size 1 μm), and $Mg(ClO_4)_2$ (CP grade, <100 μm) served as the initial precursor for the synthesis of magnesium aluminate spinel. The powders were weighed in a stoichiometric proportion (50 mol % MgO/50 mol % Al_2O_3). Magnesium aluminate spinel was synthesized using magnesium powder and magnesium perchlorate as a solid oxidizer. The experiments were conducted in compressed air at a pressure of 5 MPa. In this work, magnesium powder was used for MAS synthesis, as it allows single-phase powders with a lower magnesium perchlorate content to be obtained. The resulting single-phase MAS powders were used for subsequent sintering to produce dense ceramics.

To ensure homogeneity, all mixtures were ball milled for 4 h. Batches of the reactive mixtures (20 g) with a bulk density of ~1.1 g/cm^3 were placed in a paper cup made of ashless filter paper (d = 20 mm, H = 70 mm). The thermal profiles and the velocities of combustion were recorded using two W–Re thermocouples. The reactor was evacuated and then filled with high-purity nitrogen (>99.9%) (for the synthesis of AlON and MgAlON) or compressed air (for the synthesis of $MgAl_2O_4$) at

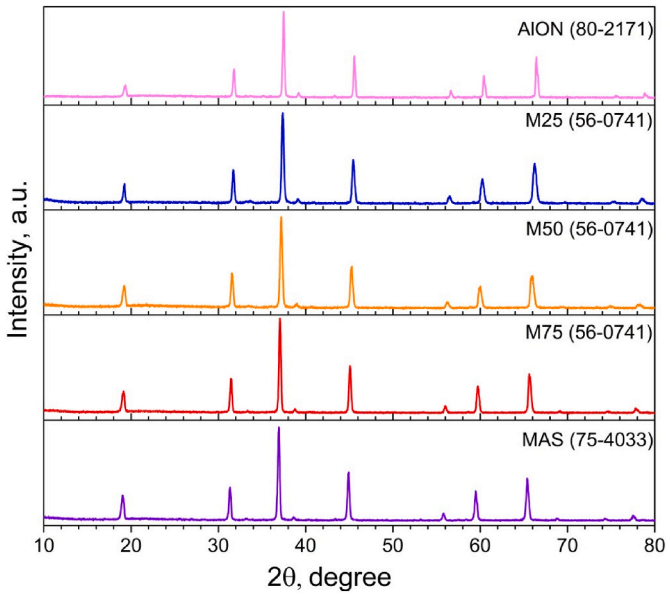

Fig. 1. XRD patterns of the as-synthesized powders.

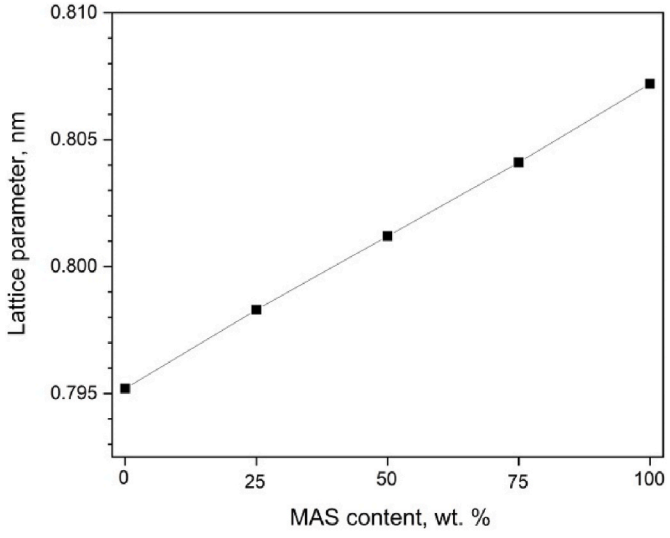

Fig. 2. The lattice parameter of the SHS powders.

Table 2
The lattice parameters of the synthesized phases and the specific surface area of the powders before and after milling.

Composition	Lattice parameter, nm	Specific surface area before milling, m^2/g	Specific surface area after milling, m^2/g
AlON	0.7952	2.9	17.7 ± 1.2
MgAlON M25	0.7983	3.2	18.5 ± 1.4
MgAlON M50	0.8012	2.9	19.2 ± 1.5
MgAlON M75	0.8041	3.6	20.5 ± 1.1
MAS	0.8071	3.8	24.6 ± 1.4

pressures of 8 MPa for AlON and 5 MPa for MgAlON and $MgAl_2O_4$. An 80% Ni–20% Cr wire coil initiated the ignition of the reactive mixtures via Joule heating. After cooling, the products were crushed and sifted using a 150-μm sieve.

2.2. Powder characterization

An X-ray diffraction analysis with Cu-Kα radiation was conducted using a Dron-3M diffractometer (Burevestnik, Russia) in the 2θ range of 10–80°. The XRD patterns were analyzed using the PDF2 database. The lattice parameters were calculated using Si as an internal standard by the Rietveld refinement method. Scanning electron microscopy (SEM) images were obtained using a Supra 50VP microscope (Carl Zeiss, Germany) with an INCA Energy + Analyzer EDS attachment (Oxford Instruments, UK). The specific surface area of the powders was evaluated using the BET method. The nitrogen content was determined using a TC-600 analyzer (Leco, USA) by inert gas fusion-thermal conductivity detection. The oxidation resistance of the powders in air was assessed via thermogravimetric analysis (TGA) using a Setaram Setsys EVO 16 instrument (Setaram, France). The samples were heated in an air flow of 50 mL/min to 1300 °C at a rate of 10 °C/min, followed by annealing at 1300 °C for 1 h.

2.3. Ceramic consolidation and characterization

For sintering, the AlON, MgAlON, and $MgAl_2O_4$ powders with the addition of sintering aids were ball milled in isopropyl alcohol at 350 rpm for 6 h. After milling, the powders were dried at 80 °C for 4 h and sieved through a 40-μm sieve. Batches (3.5 g) of the processed mixtures were uniaxially pressed into cylinders (d = 20 mm) at a pressure of 20 MPa and then cold isostatically pressed at 150 MPa. The cylinders were then sintered in a graphite furnace in a N_2 environment at different temperatures (1830, 1880, and 1930 °C) for 10 h. The sintered samples were ground and polished on both sides down to thickness of 1.5 mm.

The density of the sintered samples was measured using the Archimedes method. The Raman spectra were obtained using a custom-built spectral setup operating in the range from room temperature to 1000 °C in controlled gas atmospheres. The experimental setup was described in detail elsewhere [36,37]. A 532-nm laser was used as the excitation source, and the recording system was based on a CCD camera with liquid nitrogen cooling. Thermal diffusivity (α) was determined using an LFA 447 NANOFLASH instrument (NETZSCH, Germany) on cylindrical specimens with a diameter of 12.7 mm and a thickness of 1.5 mm in the temperature range from 25 °C to 300 °C. The thermal expansion measurements were carried out on rectangular samples using a vertical alumina dilatometer Linseis L75 (Linseis, Germany) at a constant heating/cooling rate of 3 K/min in flowing air.

The hardness (H) and Young's modulus (E) were determined using a Nano Hardness Tester (CSM Instruments, Switzerland) with the Indentation 3.0 software. The measurements were performed using a Berkovich-type diamond indenter, with a load of 10 mN, a linear loading/unloading speed of 20 mN/min, and a dwell time of 5 s. The indentation curves were analyzed using the Oliver-Farrar method (ISO 14577–1:2002); the distance between the indentations was ≥8 μm. The Vickers hardness was measured using an HVS-50 hardness tester (TimeGroup Inc., China) with an indenter load of ~9.8 N. The fracture toughness (K_{1C}) was determined via the Palmqvist method [38] according to the length of cracks propagating from the indent corners after indentation. Since crack length (c) was greater than half-diagonal of the indent (d/2) by more than 2.5 times [39,40], the Evans model (2) [41] was used for the calculations:

$$K_{1C} = 0.16 \cdot \left(\frac{d}{2}\right)^2 \cdot c^{-\frac{3}{2}} \cdot HV_1 \quad (2)$$

The optical transmittance was measured using a Vertex 80V FT-IR spectrometer (Bruker, USA) in the 1500–6500 nm range.

Table 3
The results of the EDX analysis of the SHS-derived powders.

Composition	Mg, at. %	Al, at. %	O, at. %	N, at. %	Mg/Al Nominal value	Mg/Al EDX
AlON	0	38.82	53.15	8.03	0	0
MgAlON M25	3.25	37.32	53.41	6.02	0.1	0.09
MgAlON M50	5.91	36.06	54.31	3.73	0.2	0.17
MgAlON M75	10.25	32.02	54.49	2.24	0.34	0.31
MAS	15.35	32.87	51.78	0	0.5	0.47

3. Results and discussion

3.1. Phase composition and morphology of the SHS powders

Table 1 summarizes the calculated compositions for each compound (AlON, MgAlON M25, MgAlON M50, MgAlON M75, and MAS). The XRD analysis (Fig. 1) confirms that all synthesized materials are single-phase. All XRD patterns are similar, indicating that the materials have the same cubic crystal structure (space group Fd3m). The lattice parameters of the crystalline phases determined from the XRD data are presented in Fig. 2 and Table 2. The lattice parameter increases from AlON to MAS. Fig. 2 shows the experimental lattice parameters of the synthesized powders as a function of the nominal MAS content. The experimental points deviate

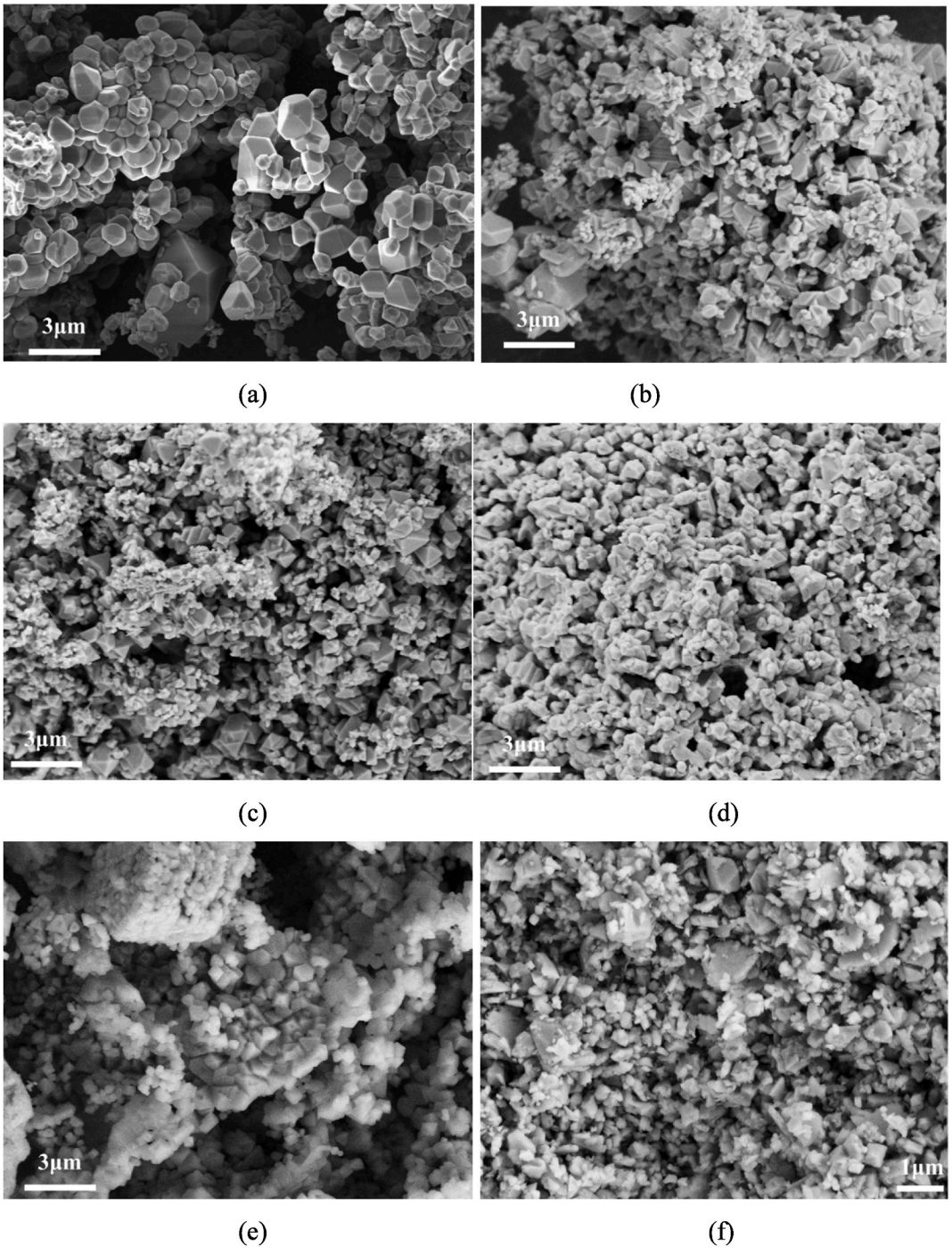

Fig. 3. SEM images of the as-synthesized AlON (a), M25 (b), M50 (c), M75 (d), MAS (e) and ball-milled AlON (f) powders.

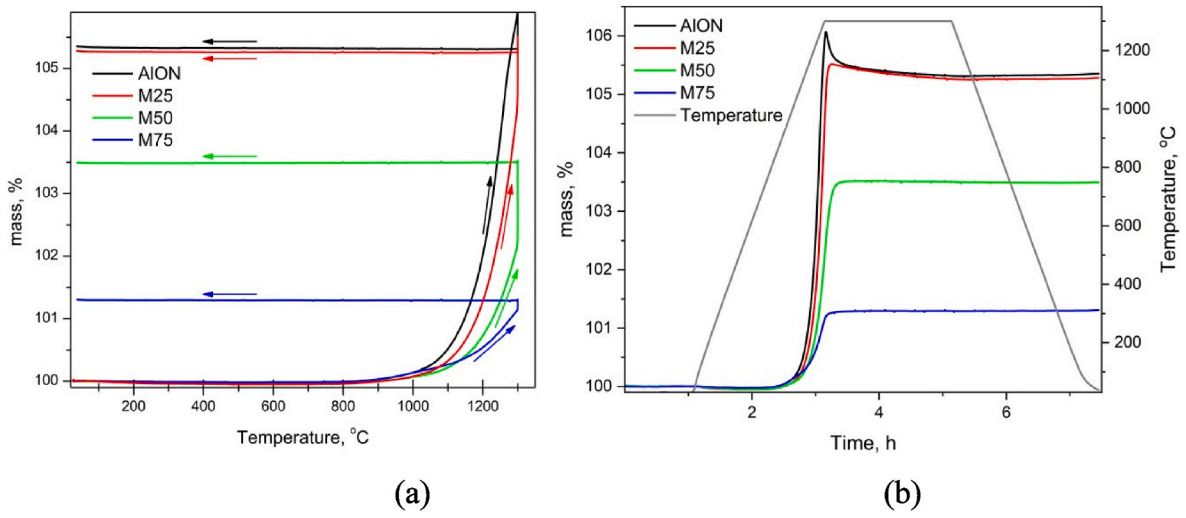

Fig. 4. Weight changes in the nitrogen-containing powders as a function of temperature (a) and time (b). Arrows in (a) indicate the direction of the temperature change.

Table 4
Nitrogen content in the synthesized SHS powders.

Compound	Nitrogen content, wt. % (calculated)	Nitrogen content, wt. % (experimental)
AlON	6.23	6.18 ± 0.5
MgAlON M25	4.67	4.75 ± 0.5
MgAlON M50	3.12	3.46 ± 0.5
MgAlON M75	1.56	1.72 ± 0.5

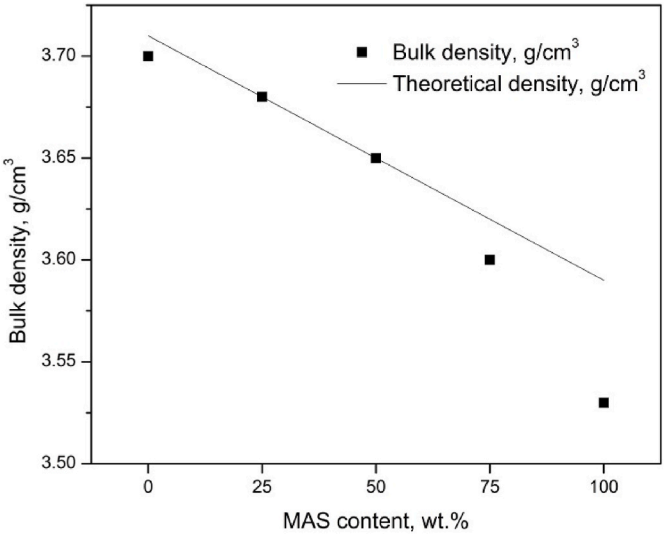

Fig. 5. The bulk density of the samples sintered at 1880 °C using a 0.2 wt % LMY additive.

from the reference values calculated from the lattice parameter of AlON (0.7950 nm) and MAS (0.808 nm) reported in the literature, suggesting a progressive shift in the actual composition relative to the nominal one. This behavior may be attributed to partial magnesium volatilization during synthesis, which is known to affect the Mg/Al ratio in Mg-containing spinels. It is well documented that the lattice parameter of MAS decreases with an increasing Al_2O_3 content [42]. The EDX analysis

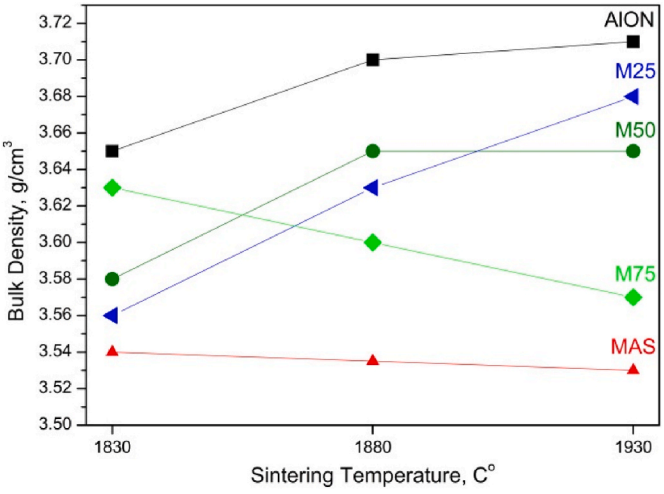

Fig. 6. The dependence of the bulk density of the samples with a 0.2 wt % LMY additive on sintering temperature.

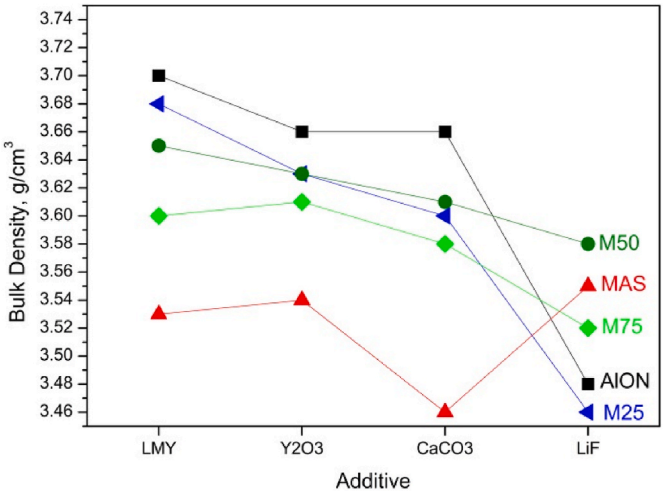

Fig. 7. The bulk density of the ceramics sintered at 1880 °C with different sintering additives.

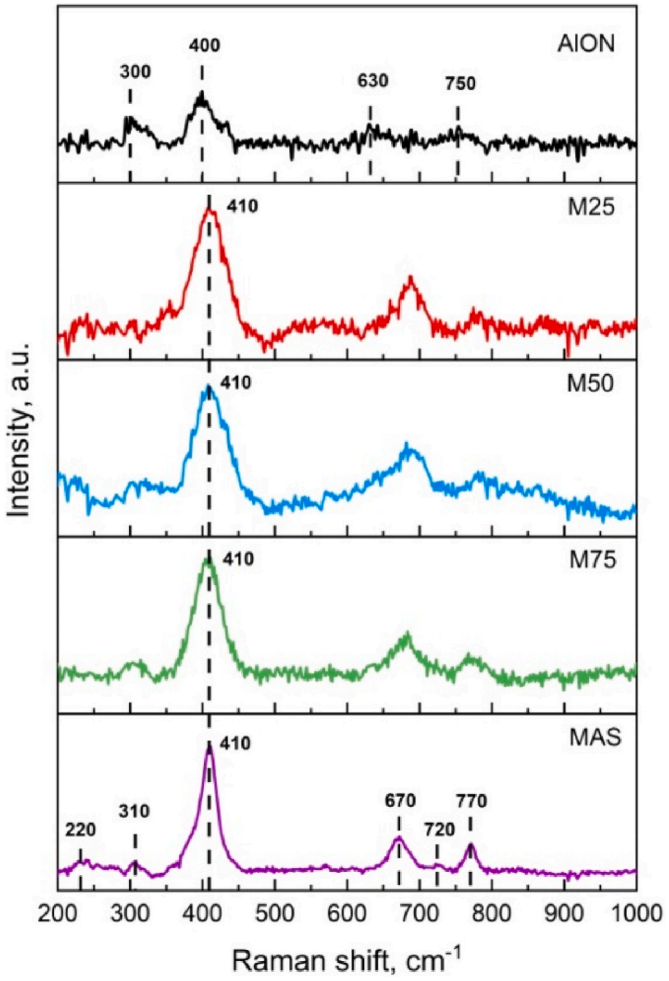

Fig. 8. Raman spectra of the ceramic samples sintered at 1880 °C with the LMY additive.

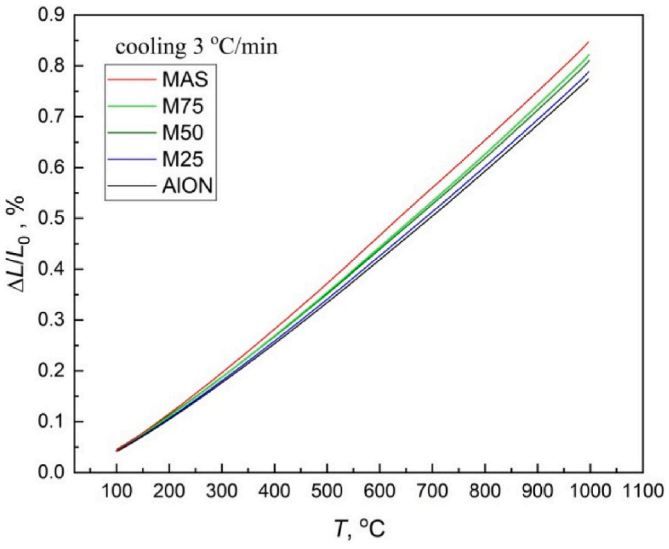

Fig. 9. Dilatometric curves of the ceramics in air. L_0 is the sample length at room temperature.

(Table 3) revealed a reduction in the Mg/Al ratio in the synthesized powders, with a magnesium content decreasing by up to 10 at % relative to the nominal value. However, due to the wide homogeneity range of the system, this volatilization did not affect the phase composition, and the XRD analysis (Fig. 1) confirmed that the powders were single-phase.

Table 5
Average linear thermal expansion coefficients of the ceramics in air.

Composition	T, °C	TEC × 10^6, K^{-1}
MAS	200-400	8.33 ± 0.03
	400-700	9.33 ± 0.02
	700-1000	9.64 ± 0.03
M75	200-400	7.90 ± 0.03
	400-700	8.86 ± 0.02
	700-1000	9.64 ± 0.02
M50	200-400	7.78 ± 0.03
	400-700	8.70 ± 0.02
	700-1000	9.46 ± 0.02
M25	200-400	7.60 ± 0.03
	400-700	8.54 ± 0.02
	700-1000	9.28 ± 0.02
AlON	200-400	7.48 ± 0.03
	400-700	8.40 ± 0.02
	700-1000	9.11 ± 0.02

The powder materials were ground in a planetary mill for further sintering. During milling, various sintering additives were introduced into the powders: 0.5 wt % Y_2O_3, 0.6 wt % $CaCO_3$, 1 wt % LiF, and a 0.2 wt % mixture of lanthanum (0.02 wt %), yttrium (0.08 wt %), and magnesium (0.1 wt %) oxides (labeled as LMY). Table 2 lists the specific surface area of the powders before and after milling. The specific surface area increases progressively with the MAS content, from 2.85 m^2/g for AlON to 3.8 m^2/g for MAS. This trend correlates with the decreasing synthesis temperature required for compositions with a higher MAS content. A higher synthesis temperature leads to an increase in the particle size [24]. Table 2 shows that the specific surface area of the materials after grinding is greater for materials with a higher initial specific surface area under the same grinding conditions. Fig. 3 shows that the as-synthesized powders consist of uniform particles with a grain size up to 3 μm. A slight decrease in the grain size is observed with an increasing MAS content. After ball milling, the powder consists of fragmented particles with a size ranging from 300 nm to 1 μm (Fig. 3f).

Thermogravimetric analysis (TGA) of nitrogen-containing powders (Fig. 4) reveals that oxidation begins at 800–850 °C for all compositions. The time dependence of mass showed that 1 h of exposure was sufficient for complete oxidation of the powders. The decrease in the mass following the maximum gain, particularly pronounced in the AlON and M25, can be explained by a two-stage oxidation mechanism of aluminum oxynitride (AlON). This mechanism is well-established in the literature [43–46] and is analogous to that reported for other oxynitride systems, such as titanium oxynitride [47]. Upon heating, oxygen is intercalated by the AlON lattice. This leads to the formation of a metastable transitional phase known in the literature as γ′-AlON. This phase retains the spinel structure but has an expanded lattice parameter due to the substitution of nitrogen by oxygen and the partial retention of nitrogen within the lattice. This process of the binding of oxygen from the gas phase directly leads to the observed mass increase. Upon further temperature increase or exposure at elevated temperature, decomposition processes become activated. Nitrogen remaining in the lattice of the metastable γ′-AlON phase begins to escape as a gas. Concurrently, the transitional spinel phase gradually transforms into the stable α-Al_2O_3 (corundum) phase. The release of gaseous nitrogen directly results in the mass loss observed in the second stage. This effect was reproducible for several samples measured with various heating rates. The reduced amplitude of this effect in the M25, M50, and M75 is attributed to their higher content of a stable oxide phase.

The nitrogen content in the synthesized powders was determined by chemical analysis. Table 4 shows that the experimental values are close to the calculated ones based on the initial mixture compositions. This

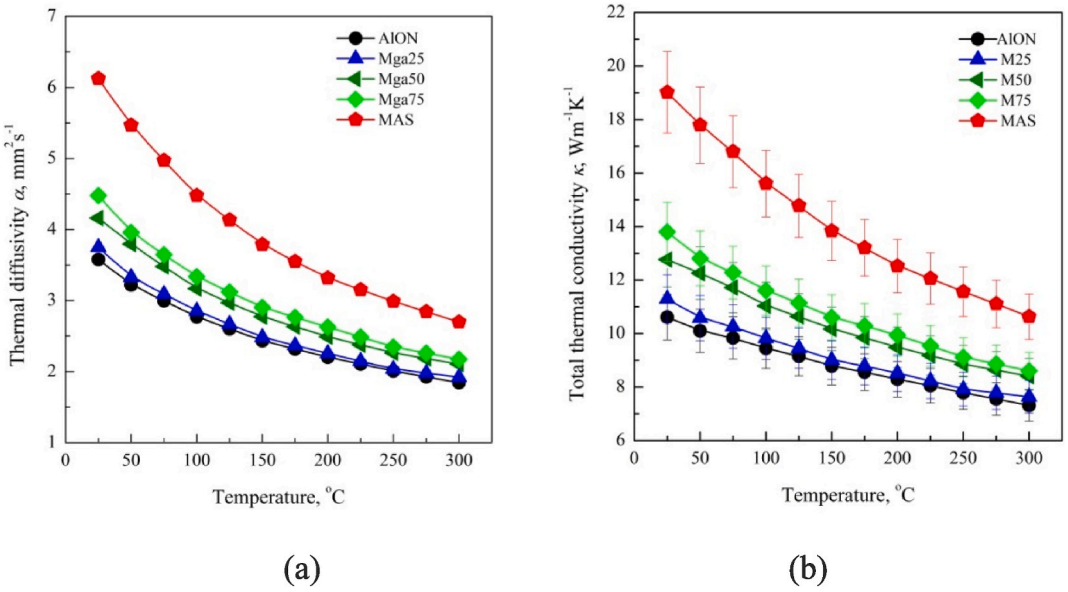

Fig. 10. Temperature dependencies of the thermal diffusion coefficient (a) and thermal conductivity (b) of the samples obtained at 1880 °C with the LMY additive.

confirms that the process of synthesis preserves the nominal nitrogen content within the experimental error.

3.2. Sintering of the SHS powders

Sintering experiments were performed at three different temperatures: 1830 °C, 1880 °C, and 1930 °C. Fig. 5 shows the bulk density of ceramics sintered at 1880 °C for 10 h with the LMY additive. The line in Fig. 5 denotes the theoretical density calculated from literature values for AlON and MAS [43,48]. The deviation from the theoretical density increases with an increasing MAS content. This is likely due to intensifiedmagnesium volatilization at higher sintering temperatures, which leads to decomposition and reduced densification.

Fig. 6 shows the effect of sintering temperature on the bulk density for the samples with the LMY additive. For MAS and M75 the density decreases at higher sintering temperatures, which is consistent with enhanced magnesium volatilization.

The effect of sintering additives on densification (Fig. 7) varies significantly with composition. For AlON, the highest density was achieved with the LMY additive, although Y_2O_3 and $CaCO_3$ also yielded relatively high densities. The maximum density for MgAlON was also achieved using the LMY additive. In contrast, the highest densities for MAS ceramics were achieved with the LiF, Y_2O_3, and LMY additives. These results demonstrate that lithium fluoride is ineffective for nitrogen-containing compositions, whereas the LMY additive is universally effective across all the compositions under study.

3.3. Properties of consolidated ceramics

Fig. 8 shows the Raman spectra of the ceramics sintered with the LMY additive at 1880 °C. For MAS, six main Raman peaks are observed at approximately 220, 310, 410, 670, 720, and 770 cm^{-1}. The peaks at ~310, 410, 670, and 770 cm^{-1} correspond to the internal vibrations of MgO_4 structural units [49]. The modes at ~220 and 720 cm^{-1} can be assigned to the symmetric Al–O stretching vibrations of AlO_4 groups, which result from cation disordering during high-temperature annealing [50]. The main modes at ~410, 670, and 770 cm^{-1} broaden as the amount of magnesium in the compositions decreases (from MAS to M25). The modes at 670 and 770 cm^{-1} shift to higher wavenumbers (680 and 780 cm^{-1}, respectively) with a decreasing magnesium content. For the M25 composition, the mode at ~310 cm^{-1} nearly disappears. For AlON, two main peaks are observed at 300 and 400 cm^{-1}. The Raman spectrum of cubic AlON consists of a number of phonon modes at approximately 300, 400, 630, 750, and 915 cm^{-1} that are related to the 3T2g, Eg, and A1g modes of spinel [51]. The mode at 915 cm^{-1} is the weakest one compared to the other phonon modes in AlON. The overall intensity of the AlON spectrum is low, and the peak around 915 cm^{-1} cannot be observed. No statistically significant differences are observed between the Raman spectra of the samples sintered at 1830 °C and 1930 °C.

The dilatometric curves of all the studied ceramics are smooth with no breaks, indicating the absence of phase transitions (Fig. 9). The average thermal expansion coefficients (TECs) calculated from the dilatometric data vary in the range of (7.5 - 9.6) $\times 10^{-6}$ K^{-1} (Table 5) and increase on heating and from AlON to MAS. These TEC values are in good agreement with the literature data on AlON [52,53] and $MgAl_2O_4$ ([54] and references cited therein).

Fig. 10 shows the dependence of the thermal diffusivity coefficient (a) and thermal conductivity (b) on temperature in the range from 25 °C to 300 °C. Thermal diffusivity typically decreases with an increasing temperature [55]. This trend is consistent with our observations for all the compositions under study. MAS exhibits higher thermal diffusivity than the other compositions. AlON exhibits the lowest thermal diffusivity among all the compositions under study. It is impossible to attribute unambiguously the changes in the thermal conductivity and diffusivity to either nitrogen or magnesium content, as both vary simultaneously. Since the ceramic samples can be considered non-porous, the main influence on the thermal diffusion coefficient may be the theoretical density of the material or its phase composition. These trends correlate with the theoretical density: materials with lower density exhibit higher thermal diffusivity. A similar dependency was found for thermal conductivity (Fig. 10b). The thermal conductivity of AlON at 300 K is 10.6 ± 1 W m^{-1} K^{-1}, increasing progressively from AlON to MAS and reaching 19 ± 1.5 W m^{-1} K^{-1} for MAS. These values are consistent with literature reports [56,57].

The in-line transmittance was measured on samples with a thickness of 1.5 mm polished on both sides. Fig. 11 shows the in-line transmittance spectra of the samples with the LMY additive obtained at different temperatures in the IR-range. The effect of sintering temperature on transmittance varies significantly with composition. The optimal sintering temperature decreases with an increasing MAS content in MgAlON compositions. These trends correlate with the observed weight loss and variations in the bulk density.

Sintering additives also have various effects on the light

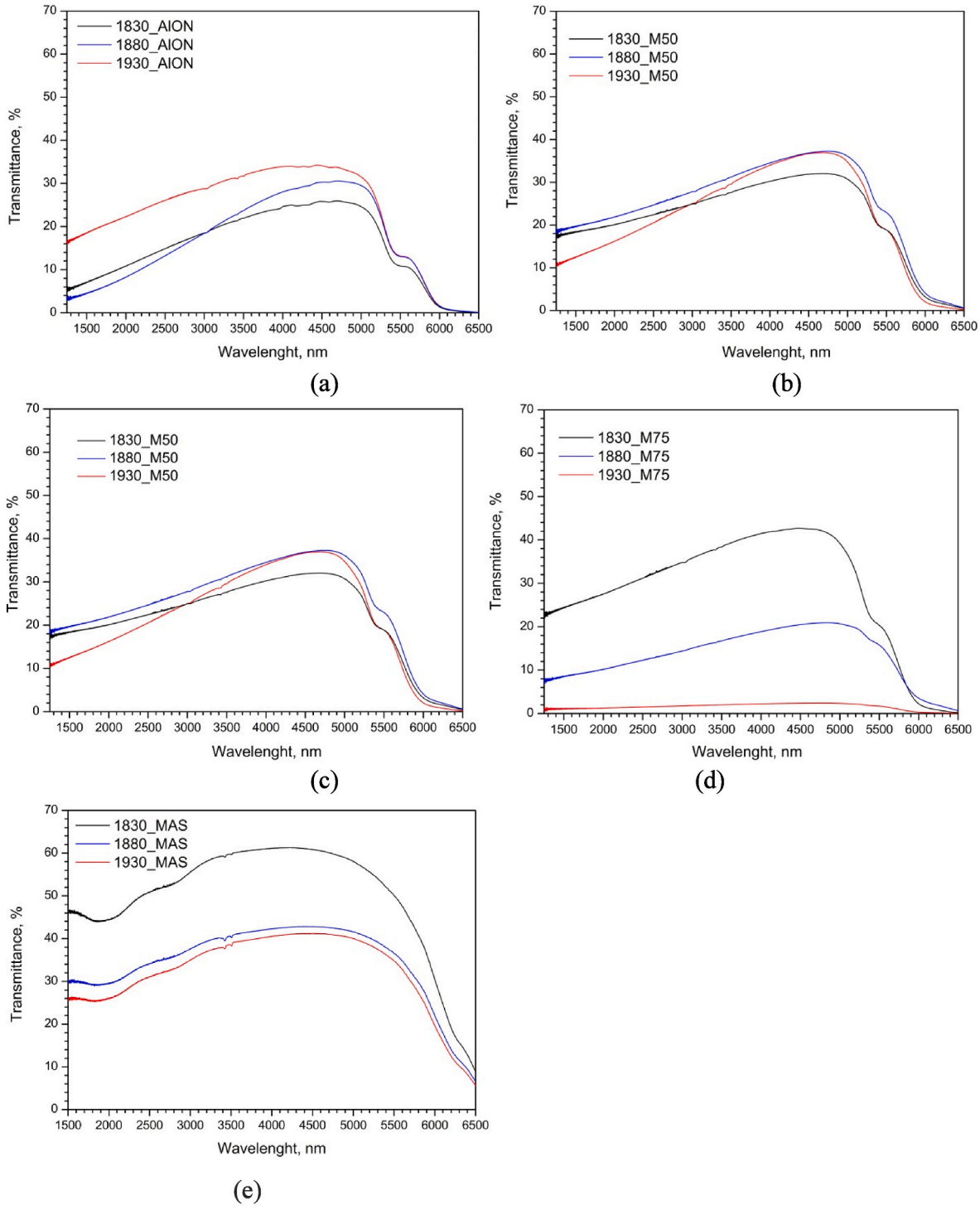

Fig. 11. The in-line transmittance of the samples derived at different temperatures with the LMY additive: AlON (a), M25 (b), M50 (c), M75 (d), and MAS (e).

transmittance of ceramics depending on their composition. Fig. 12 depicts the light transmittance of ceramics with different additives. For AlON, the highest transmittance (up to 60%) was achieved with 0.6 wt % $CaCO_3$. However, the addition of $CaCO_3$ to MgAlON resulted in complete opacity. The most effective additive for MgAlON was found to be 0.2 wt % LMY. Yttrium oxide (0.5 wt %) yielded a maximum transmittance of up to 20% for all compositions. Lithium fluoride was ineffective for all nitrogen-containing compositions. The addition of LiF to MAS resulted in a transmittance of up to 60%.

Fig. 13 illustrates the in-line transmittance of the best samples of all compositions. MAS ceramics exhibit a broader transmittance range extending to 6500 nm, whereas MgAlON M75 (with the lowest nitrogen content) shows a narrower range, which may be critical for certain applications.

The transmittance values obtained in this study (up to 61% for MAS, 57% for AlON, and 51% for MgAlON) are lower than the best reported values for HIPed or hot-pressed ceramics, which typically exceed 80%. This difference can be attributed primarily to technological aspects of the pressureless sintering process rather than to fundamental limitations of the SHS-derived powders. Despite these limitations, it is important to note that all the samples derived from the SHS powders achieved >99% relative density, demonstrating excellent sinterability comparable to

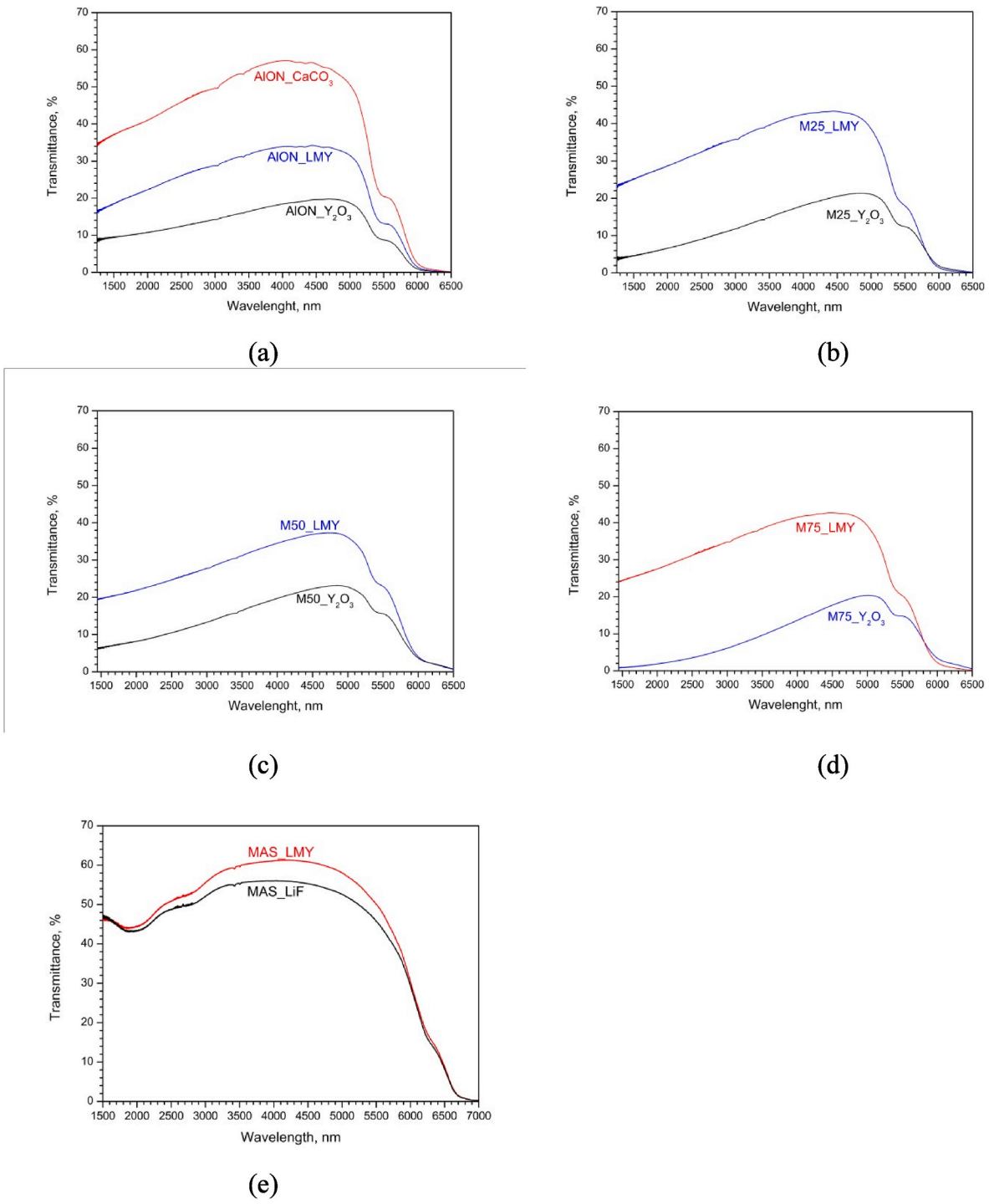

Fig. 12. The in-line transmittance of the samples derived at 1930 °C for AlON (a), 1880 °C for M25 (b) and M50 (c), and 1830 °C for M75 (d) and MAS (e).

powders produced by conventional methods.

The mechanical properties of the ceramics were evaluated using the samples obtained with the LMY additive at a sintering temperature of 1880 °C, which excluded the influence of the additive composition and sintering temperature on the mechanical properties (Table 6). The maximum hardness Hv_1 was 16.8 GPa for AlON, with a gradual decrease to 11.9 GPa for MAS ceramics.

4. Conclusions

The consolidation behavior of the SHS-derived AlON, MgAlON (three compositions), and $MgAl_2O_4$ (MAS) powders has been investigated. As a result the relationships between the composition, processing conditions, and the resulting optical, thermal, and mechanical properties have been established. The following conclusions can be drawn:

(1) Single-phase AlON, MgAlON, and MAS powders have been successfully synthesized using SHS with $Mg(ClO_4)_2$ as an internal oxidizer. The lattice parameters increase progressively from 0.7952 nm (AlON) to 0.8071 nm (MAS), which is consistent with the incorporation of Mg^{2+} into the spinel structure.

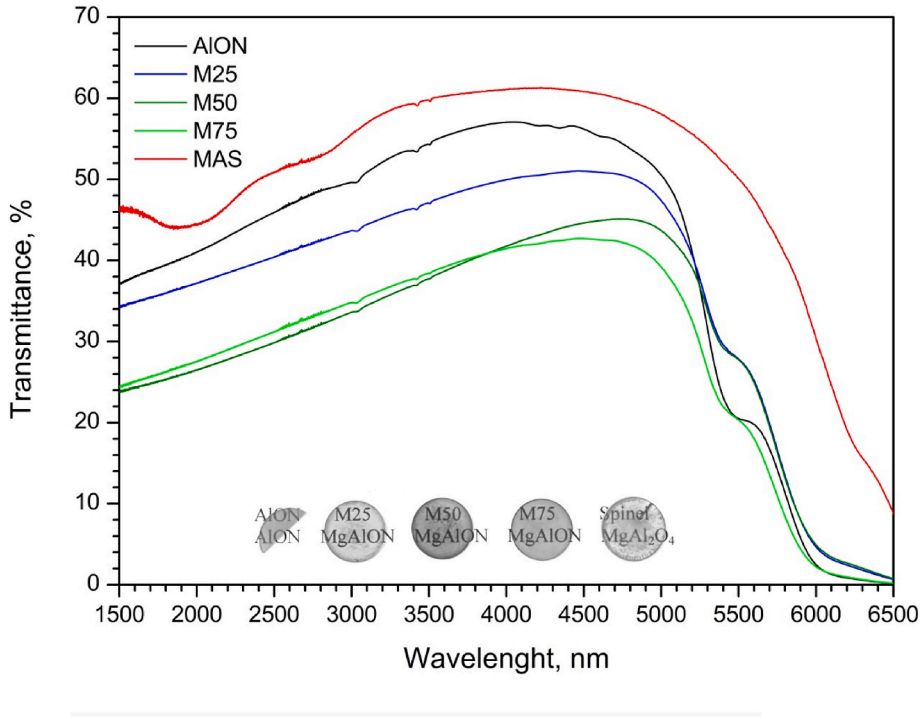

Fig. 13. The in-line transmittance and the photo of the best samples of AlON, MgAlON, and MAS.

Table 6
The Vickers hardness HV_1, fracture toughness K_{1c}, nanohardness, and Young's modulus of the sintered ceramics.

Compound	HV_1, GPa	K_{1c}, MPa·√m	H, GPa	E, GPa
AlON	16.8 ± 0.2	2.3 ± 0.1	32.3 ± 0.5	345.7 ± 0.1
MgAlON M25	15.2 ± 0.2	2.2 ± 0.1	30.1 ± 0.5	330.6 ± 0.1
MgAlON M50	14.2 ± 0.5	2.1 ± 0.1	29.3 ± 0.5	312.2 ± 0.1
MgAlON M75	13.6 ± 0.2	1.9 ± 0.1	25.5 ± 0.5	284.3 ± 0.1
MAS	11.9 ± 0.3	1.7 ± 0.1	22.2 ± 0.5	245.2 ± 0.1

(2) The optimal sintering temperature decreases with an increasing MAS content, from 1930 °C for AlON to 1830 °C for MAS. At higher temperatures, magnesium volatilization occurs in Mg-rich compositions, reducing both the density and transmittance.
(3) The effectiveness of the sintering additives depends on the composition. LMY (0.2 wt % La_2O_3-Y_2O_3-MgO) is universally effective. $CaCO_3$ (0.6 wt %) works for AlON (57% transmittance) but renders MgAlON opaque. LiF (1 wt %) is optimal for MAS (61% transmittance) but is ineffective for nitrogen-containing compositions. Finally, Y_2O_3 (0.5 wt %) yields moderate transmittance (≤20%) for all compositions.
(4) The thermal expansion coefficients increase with MAS content and temperature, ranging from (7.5–9.1) × 10^{-6} K^{-1} for AlON to (8.3–9.6) × 10^{-6} K^{-1} for MAS at 200–1000 °C. Smooth dilatometric curves indicate no phase transitions.
(5) The thermal conductivity at 25 °C increases progressively from AlON (10.6 ± 1 W m^{-1} K^{-1}) to MAS (19 ± 1.5 W m^{-1} K^{-1}), which correlates with a decreasing nitrogen content and an increasing theoretical density.
(6) The mechanical properties degrade with an increasing MAS content. The Vickers hardness decreases from 16.8 ± 0.2 GPa (AlON) to 11.9 ± 0.3 GPa (MAS), the fracture toughness from 2.3 ± 0.1 to 1.7 ± 0.1 MPa $m^1/^2$, and Young's modulus from 345.7 ± 0.1 to 245.2 ± 0.1 GPa.
(7) The established composition–property relationships enable material selection for specific applications: AlON for maximum hardness (e.g., armor applications), MAS for the highest thermal conductivity and broadest IR transmittance (e.g., optical components), and MgAlON for tailored intermediate properties.

CRediT authorship contribution statement

T.G. Akopdzhanyan: Writing – original draft, Supervision, Project administration, Methodology, Investigation, Conceptualization. **D.I. Abzalov:** Writing – review & editing, Investigation, Conceptualization. **D.A. Agarkov:** Writing – review & editing, Methodology, Investigation. **E.V. Tsipis:** Writing – review & editing, Investigation, Conceptualization. **D.S. Katrich:** Writing – review & editing, Investigation, Conceptualization. **M.I. Petrzhik:** Investigation. **K.A. Shcherbakova:** Writing – review & editing, Methodology, Investigation. **V.V. Grachev:** Writing – review & editing.

Declaration of competing interest

The authors declare that they have no known competing financial interests or personal relationships that could have appeared to influence the work reported in this paper.

Acknowledgments

This work was supported by the Russian Science Foundation (project no. 24-79-00289).

The use of equipment provided by the Scientific Facility Center at the Osipyan Institute of Solid State Physics RAS is gratefully acknowledged.

References

[1] A.M. Tsabit, D.H. Yoon, Review on transparent polycrystalline ceramics, J. Korean Ceram. Soc. 59 (2022), https://doi.org/10.1007/s43207-021-00140-6.
[2] J. McCauley, P. Patel, M. Chen, G. Gilde, E. Strassburger, B. Paliwal, K.T. Ramesh, D. Dandekar, AlON: a brief history of its emergence and evolution, J. Eur. Ceram. Soc. 29 (2009) 223–236, https://doi.org/10.1016/j.jeurceramsoc.2008.03.046.
[3] I. Ganesh, A review on magnesium aluminate (MgAl2O4) spinel: synthesis, processing and applications, Int. Mater. Rev. 58 (2013) 63–112, https://doi.org/10.1179/1743280412Y.0000000001.

[4] Z. Feng, J. Qi, X. Huang, X. Guo, Y. Yu, X. Cao, Y. Wang, D. Wu, C. Meng, T. Lu, Planetary ball-milling of AlON powder for highly transparent ceramics, J. Am. Ceram. Soc. 102 (2019) 2377–2389, https://doi.org/10.1111/jace.16146.
[5] M. Ish-Shalom, Formation of aluminium oxynitride by carbothermal reduction of aluminium oxide in nitrogen, J. Mater. Sci. Lett. 1 (1982) 147–149, https://doi.org/10.1007/BF00730944.
[6] X. Yuan, X. Liu, F. Zhang, S. Wang, Synthesis of γ-AlON powders by a combinational method of carbothermal reduction and solid-state reaction, J. Am. Ceram. Soc. 93 (2010) 22–24, https://doi.org/10.1111/j.1551-2916.2009.03380.x.
[7] H. Li, P. Min, N. Song, A. Zhang, J. Zhou, H. Xian, H. Liu, J. Fang, Rapid synthesis of AlON powders by low temperature solid-state reaction, Ceram. Int. 45 (2019) 8188–8194, https://doi.org/10.1016/j.ceramint.2019.01.121.
[8] L. Ren, H. Wang, B. Tu, X. Zong, W. Wang, Z. Fu, Investigation on composition-dependent properties of Mg5xAl23−5xO27+5xN5−5x ($0 \leq x \leq 1$): part I. optical properties via first-principles calculations, J. Eur. Ceram. Soc. 41 (2021) 1543–1549, https://doi.org/10.1016/j.jeurceramsoc.2020.10.013.
[9] B. Ma, W. Zhang, Y. Wang, X. Xie, H. Song, C. Yao, Z. Zhang, Q. Xu, Hot isostatic pressing of MgAlON transparent ceramic from carbothermal powder, Ceram. Int. 44 (2018) 4512–4515, https://doi.org/10.1016/j.ceramint.2017.12.023.
[10] A. Schramm, M. Thümmler, O. Fabrichnaya, S. Brehm, J. Kraus, J. Kortus, D. Rafaja, C. Scharf, C.G. Aneziris, Reaction sintering of MgAlON at 1500 °C from Al2O3, MgO and AlN and its wettability by AlSi7Mg, Crystals 12 (2022), https://doi.org/10.3390/cryst12050654.
[11] X. Sun, X. Jiang, Y. Shan, X. Han, J. Xu, J. Li, Low-temperature solid reaction synthesis of high sinterability MgAl2O4 powder from γ-Al2O3+MgO and θ/α-Al2O3+MgO batches, Ceram. Int. 48 (2022) 17471–17480, https://doi.org/10.1016/j.ceramint.2022.03.011.
[12] A. Alhaji, M.H. Taherian, S. Ghorbani, S.A. Sharifnia, Development of synthesis and granulation process of MgAl2O4 powder for the fabrication of transparent ceramic, Opt. Mater. 98 (2019), https://doi.org/10.1016/j.optmat.2019.109440.
[13] E.H. Song, Y.Y. Zhou, Y. Wei, X.X. Han, Z.R. Tao, R.L. Qiu, Z.G. Xia, Q.Y. Zhang, A thermally stable narrow-band green-emitting phosphor MgAl2O4:Mn2+ for wide color gamut backlight display application, J. Mater. Chem. C 7 (2019) 8192–8198, https://doi.org/10.1039/c9tc02107h.
[14] X. Li, H. Yu, F. Yao, H. Ni, R. Sun, J. Zhou, J. Ding, J. Li, Q. Zhang, Insight into site occupancy of cerium and manganese ions in MgAl2O4 and their energy transfer for dual-mode optical thermometry, J. Alloys Compd. 928 (2022), https://doi.org/10.1016/j.jallcom.2022.166701.
[15] N. Thanabodeekij, M. Sathupunya, A.M. Jamieson, S. Wongkasemjit, Correlation of sol–gel processing parameters with microstructure and properties of a ceramic product, Mater. Charact. 50 (2003) 325–337, https://doi.org/10.1016/j.matchar.2003.08.001.
[16] P.J. Dereń, K. Maleszka-Bagińska, P. Głuchowski, M.A. Małecka, Spectroscopic properties of Nd3+ in MgAl2O4 spinel nanocrystals, J. Alloys Compd. 525 (2012) 39–43, https://doi.org/10.1016/j.jallcom.2012.02.065.
[17] S.M. Kim, A.M. Kierzkowska, M. Broda, C.R. Müller, Sol-gel synthesis of MgAl2O4-stabilized CaO for CO2 capture, in: Energy Procedia, Elsevier Ltd, 2017, pp. 220–229, https://doi.org/10.1016/j.egypro.2017.03.1164.
[18] Q. Wu, F. Jiang, G. Feng, S. Wang, L. Miao, W. Jiang, J. Liang, J. Liu, Nonhydrolytic sol-gel in-situ synthesis of high performance MgAl2O4/C adsorbent materials, Arab. J. Chem. 16 (2023), https://doi.org/10.1016/j.arabjc.2022.104393.
[19] L.R. Ping, A.-M. Azad, T.W. Dung, Magnesium aluminate (MgAl2O4) spinel produced via self-heat-sustained (SHS) technique, Mater. Res. Bull. 36 (2001) 1417–1430, https://doi.org/10.1016/S0025-5408(01)00622-5.
[20] N.N. Yen, C.H.D. Anh, B.T.N. Mai, D.Q. Khanh, L.M. Hai, C.V. Str, H.B. Trung, H. Noi, V. Nam, Preparation of MgAl 2 O 4 Nanopowder Using Combustion Synthesis Method and its Properties Tổng Hợp Bột Nano MgAl2O4 Bằng Phương Pháp Đốt Cháy Và Khảo Sát Tính Chất, Dai, 2018.
[21] S.R. Ghosh, S. Mukherjee, S. Banerjee, Solution combustion synthesis of alumina spinel and its characterization, Interceram - Int. Ceram. Rev. 67 (2018) 34–41, https://doi.org/10.1007/s42411-018-0004-5.
[22] T.G. Akopdzhanyan, S.I. Rupasov, S. Vorotilo, Chemically activated combustion synthesis of AlON under high nitrogen pressure, Combust. Flame 232 (2021) 111560, https://doi.org/10.1016/j.combustflame.2021.111560.
[23] T.G. Akopdzhanyan, I.P. Borovinskaya, E.A. Chemagina, Aluminum oxynitride by SHS under high pressure of nitrogen gas, Int. J. Self-Propag. High-Temp. Synth. 26 (2017) 110–114, https://doi.org/10.3103/S1061386217020029.
[24] T. Akopdzhanyan, D. Abzalov, D. Moskovskikh, M. Abedi, V. Romanovski, Combustion synthesis of magnesium-aluminum oxynitride MgAlON with tunable composition, Materials 16 (2023), https://doi.org/10.3390/ma16103648.
[25] Y. Shan, J. Xu, G. Wang, X. Sun, G. Liu, J. Xu, J. Li, A fast pressureless sintering method for transparent AlON ceramics by using a bimodal particle size distribution powder, Ceram. Int. 41 (2015) 3992–3998, https://doi.org/10.1016/j.ceramint.2014.11.084.
[26] Y. Shan, X. Sun, B. Ren, H. Wu, X. Wei, E.A. Olevsky, J. Xu, J. Li, Pressureless sintering of highly transparent AlON ceramics with CaCO3 doping, Scr. Mater. 157 (2018) 148–151, https://doi.org/10.1016/j.scriptamat.2018.08.023.
[27] J. Wu, Z. Wang, Z. Hu, X. Liu, D. Tan, Y. Dai, D. Geng, Recent progress and challenges of transparent AlON ceramics, Trans. Nonferrous Met. Soc. China 33 (2023) 653–667, https://doi.org/10.1016/S1003-6326(22)66136-3.
[28] J. Zhang, J. Lei, Y. Shi, J. Xie, F. Lei, L. Zhang, Effect of Y2O3, La2O3 and MgO co-doping on densification, microstructure and properties of AlON ceramics, J. Ceram. Sci. Technol. 8 (2017) 177–182, https://doi.org/10.4416/JCST2016-00114.
[29] X. Chu, X. Mao, X. Li, X. Zeng, R. Tian, J. Zhang, S. Wang, Preparation of transparent MgAlON ceramics with tunable compositions, Ceram. Int. (2024), https://doi.org/10.1016/j.ceramint.2024.05.251.
[30] R. Zhang, H. Wang, M. Tian, Y. Wang, M. Liu, H. Wang, G. Zhang, Pressureless reaction sintering and hot isostatic pressing of transparent MgAlON ceramic with high strength, Ceram. Int. 44 (2018) 17383–17390, https://doi.org/10.1016/j.ceramint.2018.06.203.
[31] X. Zong, H. Wang, H. Gu, L. Ren, S. Guo, B. Tu, W. Wang, S. Liu, Z. Fu, Highly transparent Mg0.27Al2.58O3.73N0.27 ceramic fabricated by aqueous gelcasting, pressureless sintering, and post-HIP, J. Am. Ceram. Soc. 102 (2019) 6507–6516, https://doi.org/10.1111/jace.16544.
[32] A. Goldstein, A. Goldenberg, M. Hefetz, Transparent polycrystalline MgAl2O4 spinel with submicron grains, by low temperature sintering, J. Ceram. Soc. Japan 117 (2009) 1281–1283, https://doi.org/10.2109/jcersj2.117.1281.
[33] S.S. Balabanov, R.P. Yavetskiy, A. V Belyaev, E.M. Gavrishchuk, V. V Drobotenko, I.I. Evdokimov, A. V Novikova, O. V Palashov, D.A. Permin, V.G. Pimenov, Fabrication of transparent MgAl2O4 ceramics by hot-pressing of sol-gel-derived nanopowders, Ceram. Int. 41 (2015) 13366–13371, https://doi.org/10.1016/j.ceramint.2015.07.123.
[34] D.E. Deulina, V.D. Paygin, I.N. Shevchenko, S.A. Stepanov, E.S. Dvilis, O. L. Khasanov, D.T. Valiev, F. Huang, The effect of thermal annealing on mechanical and optical properties of MgAl2O4 ceramics fabricated by spark plasma sintering, Russ. Phys. J. 67 (2024) 381–387, https://doi.org/10.1007/s11182-024-03134-z.
[35] T.G. Akopdzhanyan, SHS of AlON powder under pressure of nitrogen gas: controlling product patterning, Int. J. Self-Propag. High-Temp. Synth. 29 (2020) 124–125, https://doi.org/10.3103/S1061386220020028.
[36] D.A. Agarkov, I.N. Burmistrov, F.M. Tsybrov, I.I. Tartakovskii, V. V Kharton, S. I. Bredikhin, In-situ Raman spectroscopy analysis of the interfaces between Ni-based SOFC anodes and stabilized zirconia electrolyte, Solid State Ionics 302 (2017) 133–137, https://doi.org/10.1016/j.ssi.2016.12.034.
[37] D.A. Agarkov, I.N. Burmistrov, F.M. Tsybrov, I.I. Tartakovskii, V. V Kharton, S. I. Bredikhin, Kinetics of NiO reduction and morphological changes in composite anodes of solid oxide fuel cells: estimate using Raman scattering technique, Russ. J. Electrochem. 52 (2016) 600–605, https://doi.org/10.1134/S1023193516070028.
[38] S. Palmqvist, Occurrence of crack formation during vickers indentation as a measure of the toughness of hard metals, Arch. Eisenhuettenwes (1962) 629–634.
[39] A.G. Evans, E.A. Charles, Fracture toughness determinations by indentation, J. Am. Ceram. Soc. (1976) 371–372.
[40] K. Niihara, R. Morena, D.P.H. Hasselman, Evaluation ofK Ic of brittle solids by the indentation method with low crack-to-indent ratios, J. Mater. Sci. Lett. 1 (1982) 13–16, https://doi.org/10.1007/BF00724706.
[41] Y. Guo, T. Staedler, J. Müller, S. Heuser, B. Butz, X. Jiang, A detailed analysis of the determination of fracture toughness by nanoindentation induced radial cracks, J. Eur. Ceram. Soc. 40 (2020) 276–289, https://doi.org/10.1016/j.jeurceramsoc.2019.10.013.
[42] N. Kashii, H. Maekawa, Y. Hinatsu, Dynamics of the cation mixing of MgAl2O4 and ZnAl2O4 spinel, J. Am. Ceram. Soc. 82 (1999) 1844–1848, https://doi.org/10.1111/j.1151-2916.1999.tb02007.x.
[43] N.D. Corbin, Aluminum oxynitride spinel: a review, J. Eur. Ceram. Soc. 5 (1989) 143–154, https://doi.org/10.1016/0955-2219(89)90030-7.
[44] P. Goursat, P. Goeuriot, M. Billy, Contribution a l'etude du systeme Al/O/N I — reactive de l'oxynitrure d'aluminium γ, Mater. Chem. 1 (1976) 131–149, https://doi.org/10.1016/0390-6035(76)90010-9.
[45] P. Goursat, M. Billy, P. Goeuriot, J.C. Labbe, J.M. Villechenoux, G. Roult, J. Bardolle, Contribution a l'etude du systeme AL/O/N II: retention d'azote dans les produits d'oxydation de l'oxynitrure d'aluminium γ, Mater. Chem. 6 (1981) 81–93, https://doi.org/10.1016/0390-6035(81)90046-8.
[46] X. Mao, B. Zhang, R. Qi, Y. Chen, J. Zhang, S. Wang, A thermal oxidation route for strengthening transparent AlON ceramics via transitional oxide film, J. Eur. Ceram. Soc. 46 (2026) 118272, https://doi.org/10.1016/j.jeurceramsoc.2026.118272.
[47] J. Yoo, H. Yoo, H. Jung, S. Bang, H. Kim, J. Choi, H. Suh, J.-H. Lee, J.-G. Kim, N. Hur, Titanium oxynitride microspheres with the rock-salt structure for visible-light photocatalysts, J. Mater. Chem. A 4 (2015), https://doi.org/10.1039/C5TA06758H.
[48] G. Ibram, A review on magnesium aluminate (MgAl2O4) spinel: synthesis, processing and applications, Int. Mater. Rev. 58 (2013) 63–112, https://doi.org/10.1179/1743280412Y.0000000001.
[49] Y. Ma, X. Bao, Z. Sui, X. Zhao, X. Liu, Quantifying Mg–Al cation distribution in MgAl2O4-spinel using Raman spectroscopy: an experimental calibration, Solid Earth Sci. 7 (2022) 60–71, https://doi.org/10.1016/j.sesci.2021.09.002.
[50] N. Van Minh, I.-S. Yang, A Raman study of cation-disorder transition temperature of natural MgAl2O4 spinel, Vib. Spectrosc. 35 (2004) 93–96, https://doi.org/10.1016/j.vibspec.2003.12.013.
[51] I.G. Batyrev, D.E. Taylor, G.A. Gazonas, J.W. McCauley, Density functional theory and evolution algorithm calculations of elastic properties of AlON, J. Appl. Phys. 115 (2014) 23505, https://doi.org/10.1063/1.4859435.
[52] Y. Lv, W. Zhu, M. Tang, H. Zou, G. Zu, Y. Han, X. Ran, Diffusion joining of transparent AlON ceramic using La2O3-Nb2O5-B2O3-SiO2-Al2O3 glass interlayer, Ceram. Int. 51 (2025), https://doi.org/10.1016/j.ceramint.2025.09.456.
[53] G. Quinn, N. Corbin, J. McCauley, Thermomechanical properties of aluminum oxynitride spinel, Am. Ceram. Soc. Bull. 63 (1984) 723–725, 729.
[54] W. Qiu, C. Su, Y. Liu, W. Song, Thermodynamic properties of MgAl2O4 spinel at high temperatures and high pressures, Crystals 13 (2023), https://doi.org/10.3390/cryst13020240.
[55] K. Zheng, H. Wang, B. Tu, P. Xu, B. Chen, B. Wang, W. Wang, Z. Fu, Compositional tailoring effect on crystal structure, mechanical and thermal properties of γ-AlON

transparent ceramics, J. Eur. Ceram. Soc. 42 (2022) 2983–2993, https://doi.org/10.1016/j.jeurceramsoc.2022.01.043.

[56] Y.W. Kim, Y.W. Oh, S.Y. Yoon, R. Stevens, H.C. Park, Thermal diffusivity of reaction-sintered AlON/Al2O3 particulate composites, Ceram. Int. 34 (2008) 1849–1855, https://doi.org/10.1016/j.ceramint.2007.06.004.

[57] C. Ni, H. Fan, X. Wang, M. Yao, Thermal conductivity prediction of MgAl2O4: a non-equilibrium molecular dynamics calculation, J. Iron Steel Res. Int. 27 (2020) 500–505, https://doi.org/10.1007/s42243-020-00364-6.